Journal of Physics: Energy

PAPER

Surface morphology, electronic defects and passivation strategies at the p–n junction of Cu(In,Ga)(S,Se)$_2$ solar cells

Amala Elizabeth[1,2,5], **Andreas May**[1,2,5], **Finnegan Volkamer**[1,2], **Florian Giesl**[3], **Hossam Elanzeery**[3], **Thomas Dalibor**[3], **Daniel Abou-Ras**[4] and **Harry Mönig**[1,2,*]

[1] Physikalisches Institut, Universität Münster, Wilhelm-Klemm-Strasse 10, Münster, 48149, Germany
[2] Center for Nanotechnology (CeNTech), Heisenbergstrasse 11, 48149 Münster, Germany
[3] AVANCIS GmbH, Otto-Hahn-Ring 6, 81739 Munich, Germany
[4] Helmholtz-Zentrum Berlin für Materialien und Energie GmbH, Hahn-Meitner-Platz 1, 14109 Berlin, Germany
[5] These authors contributed equally to the manuscript.
[*] Author to whom any correspondence should be addressed.

E-mail: harry.moenig@uni-muenster.de

Keywords: chalcopyrite solar cells, defect physics, surface analysis, sulfur, scanning tunneling spectroscopy

Supplementary material for this article is available online

OPEN ACCESS

RECEIVED
19 December 2024

REVISED
12 February 2025

ACCEPTED FOR PUBLICATION
21 February 2025

PUBLISHED
11 March 2025

Abstract

Based on the high power conversion efficiencies and compatibility toward large-area deposition techniques, Cu(In,Ga)(S,Se)$_2$ (CIGSSe) phototvoltaic absorbers are currently at the forefront of chalcopyrite thin-film solar cell technology. The performance of these solar cells is critically dependent on the properties of the interface between the p-type chalcopyrite absorber and the n-type buffer and window layers. Due to the complex defect physics of the chalcopyrites in general, the defect-electronic properties of the absorber surface is of particular concern. In this regard, the CIGSSe surfaces are considerably less understood compared with their S-free counterparts (e.g. Cu(In,Ga)Se$_2$). In the present work, by applying high-resolution scanning probe techniques such as atomic force microscopy and scanning tunneling spectroscopy (STS), combined with electron backscatter diffraction, the morphology, the crystallographic orientation, and the defect electronic properties of CIGSSe thin-film surfaces were investigated. Our work highlights distinct differences as well as similarities between S-containing and S-free chalcopyrite thin films. Three types of features were found on the CIGSSe surface, which were found to be exclusively made of polar facets. This is different from S-free absorbers that are known to facet in both, polar and non-polar planes with distinct electronic properties. Defect density mapping using STS revealed a highly defective surface with significant lateral inhomogeneities. Furthermore, grain boundary band bending detected in S-free absorber surfaces was absent. However, similar to S-free absorbers, annealing under ultra-high vacuum conditions was found to electronically passivate the CIGSSe surface. Our results shed light on the fundamental properties of these S-containing chalcopyrite-type surfaces and demonstrate a valuable platform for further optimization of this promising solar cell technology.

1. Introduction

Chalcopyrite-type thin-film solar cells based on Cu(In,Ga)(S,Se)$_2$ (CIGSSe) absorbers are promising candidates in the quest for viable solutions to the growing global demand for sustainable and renewable energy conversion [1]. The exceptional performance of this second generation photovoltaic technology is attributed mainly to the high absorption coefficient, the tunable direct bandgap, the long-term thermal stability, the flexibility in the device design, and the easy adaptability toward large area production of the absorber materials. In recent years, post-deposition treatments (PDTs) using alkali metals (Na, K, Rb, Cs) and alloying with Ag, etc of the chalcopyrite absorbers have significantly improved the power conversion efficiencies (PCE) of these devices. Currently, a certified record PCE of 23.64% has been achieved by

Evolar/Uppsala University for laboratory fabricated single junction solar cells based on Ag-alloyed S-free Cu(In,Ga)Se_2 (CIGSe) absorbers [2]. Furthermore, AVANCIS GmbH holds the record with a PCE of 20.3% in CIGSSe-based sub-module devices [3]. Chalcopyrite-type solar cells exhibit a multilayered device structure (glass substrate/Mo/p-type absorber/n-type buffer/window layer) with the p–n junction forming between the absorber and window layers. The device performance is strongly correlated to the properties of the absorber surface and related interfaces as electronic defects present there can lead to significant recombination losses [4]. Hence, as a prerequisite to developing strategies for device optimization, the properties of the absorber surface need to be understood. However, the polycrystalline nature of the absorber thin film generally preferred in high efficiency solar cells makes their surfaces extremely complex, making surface/interface defect studies quite challenging. Furthermore, CIGSe absorbers incorporated with additional sulfur (CIGSSe) allows for a more versatile band gap engineering [5]. Despite the recent technological advances toward using these sulfurized absorbers [3], only limited research exists concerning their surface electronic and morphological properties.

Previous studies were primarily focused on understanding the defect physics at the surfaces of Cu-poor grown S-free absorbers [6–11]. Among others, oxidation was found to be a major factor leading to detrimental electronic defects at the surface [8]. In polycrystalline chalcopyrites, a pronounced lateral inhomogeneity in the surface defect density was detected, both between different grains and between grains and grain boundaries (GBs) [12, 13]. The differences between the surface properties including defect density, work function and wetting by buffer layer were attributed to the nature of the various facet terminations [12, 14, 15]. For example, Cu-poor grown selenide-based chalcopyrites are known to form various morphological features that terminate in both polar and non-polar facets at the surface, which behave differently towards surface oxidation [12]. The polar facets were found to be easily oxidized in comparison to the non-polar facets, rendering them more defective. In this work, we investigate the surface properties of S-containing CIGSSe thin films in the context of their morphology, crystallographic facet orientations and defect physics, and discuss corresponding passivation strategies. We also draw parallels and distinctions between these materials and previously investigated S-free absorbers.

As opposed to typical integral techniques such as photoluminescence and Hall-effect measurements used to study optoelectronic defect physics of semiconductors, specialized high-resolution techniques are required to access their localized surface electronic properties. Scanning tunneling spectroscopy (STS) is an ideal technique that provides information about the localized density of states of the surface of chalcopyrite absorbers with a nanoscale spatial resolution [13, 16, 17]. In this technique based on the scanning tunneling microscope (STM), the tunneling current (I) between a sharp metallic tip and the sample surface as a function of the applied bias voltage (U) is measured. The differential conductance dI/dU approximately reflects the density of states (DOS) of the sample. Using a suitable bias voltage range covering the negative and positive polarity, the DOS in the energy range around the Fermi level can be probed. Furthermore, by recording $I(U)$ spectra at every pixel of an equally spaced grid (current imaging tunneling spectroscopy (CITS)), dI/d$U(U)$ maps are obtained, which can be analyzed to highlight lateral inhomogeneities in the surface defect density at different energies eU. From STM/STS/CITS measurements, correlations can be made between morphological features and the surface defect level density.

Electron backscatter diffraction (EBSD) based on scanning electron microscopy (SEM), is a powerful tool in crystallographic studies, providing the orientation of single grains. However, being an integral technique, EBSD should be complemented by additional analytical methods to obtain the crystallographic facet orientations at the sample surface. Here, we combine topographical information obtained from scanning probe techniques such as STM and atomic force microscopy (AFM), with EBSD measurements on identical areas to ascertain the identity of the surface facets in CIGSSe thin films. In combination with the defect density mapping by CITS, a comprehensive view of CIGSSe absorber surface properties is obtained.

In the present work, we show that the investigated CIGSSe surfaces are dominated by three distinct morphological features, all of which are comprised exclusively of polar planes ({112}, {100}/{001} etc). Interestingly, the additional electronically passivated non-polar planes that were found previously on S-free absorbers [12] are absent on CIGSSe surfaces. In fact, the surface is highly defective with significant lateral inhomogeneities, as indicated by CITS mapping. Drawing similarities between the dI/dU spectral signature in CIGSSe and those detected previously in oxidized S-free absorbers [8], we show that these surface defects appear in conjunction with oxidation-induced surface dipoles, which can be removed by annealing the sample under ultra-high vacuum (UHV) conditions. The combined analytical approach followed in this work helps to obtain a fundamental understanding of the sulfurized absorbers, relevant for optimization of high efficiency thin film chalcopyrite solar cells.

2. Experimental methods

Sample growth: The CIGSSe samples investigated in this study were processed as outlined in [18]. Its near-surface average composition (⩽50 nm information depth) is given by $GGI = [Ga]/([Ga] + [In]) \approx 0.11$ and $SSSe = [S]/([S] + [Se]) \approx 0.47$ with a Na content of approximately 1%, as confirmed by glow discharge optical emission spectroscopy (GDOES) measurements. To avoid calibration errors, these measurements were optimized as described in [19]. Within the absorber bulk (at a depth of around 2 μm), GGI increases to 0.82 while there is a noticeable decrease in the SSSe (0.11). Furthermore, analyzing the core-level intensities from surface sensitive x-ray photoelectron spectroscopy (XPS) investigations (with a typical information depth of 3–5 nm) indicated an overall increase in the S content at the surface in comparison to the bulk (see section 4 of the supplementary information (SI) for more details).

Sample transfer and handling: Following its production, the sample was stored and manipulated exclusively under inert N_2 atmosphere to ensure the preservation of the pristine surface state. Before measurements were conducted, the sample was cut into several pieces, which were washed for 225 s with double-deionized water and dried under N_2 flow. The piece designated for EBSD and AFM topographic measurements was subsequently stored and transported in air, as oxidation of the surface does not significantly alter the examined properties [20]. During the annealing step, the sample was heated to 280 °C for 30 min in UHV conditions, after which the sample was allowed to freely cool down to room temperature (RT).

STM/CITS: The STM topography and $\mathrm{d}I/\mathrm{d}U(U)$ data were acquired with a commercial VT-AFM/STM from Scienta Omicron operated at RT and at a base pressure of 10^{-9} mbar. Electrochemically etched tungsten wires (0.3 mm diameter) that formed sharp STM tips were used in these measurements. The STM topography was typically obtained at bias voltage $U = +2.0$ V and current setpoint $I = 0.23$ nA, unless stated otherwise. Current imaging tunneling spectroscopy (CITS) maps were obtained by approaching the tip to the sample surface at voltages between −2.3 V and −2.7 V, disabling the feedback loop, sweeping U from negative to positive values and measuring the corresponding I on an equally spaced grid (170 × 170 or 200 × 200 pixels). The exact voltage range used during the CITS measurements are specified in the respective figure captions. Afterwards, $\mathrm{d}I/\mathrm{d}U(U)$ data was obtained by numerical differentiation. Each CITS map took around 40 h to complete, due to which the data is prone to some lateral drift. The obtained data was analyzed with the WSxM 5.0 software [21].

XPS: Surface chemical compositional analysis was carried out using a commercial UHV system from SPECS equipped with a PHOIBOS 100 hemispherical analyzer and a delayline detector. An AlKα x-ray source was used for the measurements. For a quantitative analysis of the surface composition, the XPS core level intensities calculated by the peak areas were obtained and normalized to the corresponding sensitivity factors of our setup. This corrected intensity $\hat{I}_k^{\psi_{nl}}$ for the core-level ψ_{nl} in an element k can be equated to its concentration if the concentration is constant within the investigated depth of the sample. As this is not the case, the data is analyzed in terms of corrected intensities.

AFM: The measurements were carried out in ambient conditions using a tabletop NanoSurf NaioAFM system. Commercially available cantilevers (Tap190AI-G) manufactured by BudgetSensors were used for obtaining the topography images. All AFM measurements were recorded in dynamic mode.

EBSD: The measurements were performed using a Zeiss UltraPlus SEM with an Oxford Instruments Symmetry EBSD detector at a beam energy of 15 keV and a current of 6 nA. The data was acquired and evaluated using the software AZtec. Owing to the tetragonal crystal structure of the chalcopyrite-type absorbers, all the indices are given in the tetragonal notation unless mentioned otherwise.

3. Results and discussion

3.1. Surface morphology and crystallographic orientation

To correlate morphology and crystallographic features at the surface of CIGSSe absorbers, it is essential that all the measurements be carried out at the same region. In our experiments, this was done by making a mark on the sample surface and conducting the SEM, EBSD and AFM measurements near it. The procedure followed is explained in detail in section 1 of the SI. Figure 1(a) shows a SEM image of the area marked by a white square in the overview EBSD map in figure 1(b). Three prominent morphological features appear to dominate the surface-triangles (TR), terraces (TE) and basalt-like columns (BL) - which are marked by white ovals in the SEM image. In figure 1(c), an AFM image overlapping the SEM image in figure 1(a) is shown. Here it is noted that the partial derivative in the scan direction of the AFM topography data is shown, as it makes the identification of the different morphological features easier. Furthermore, the identical features

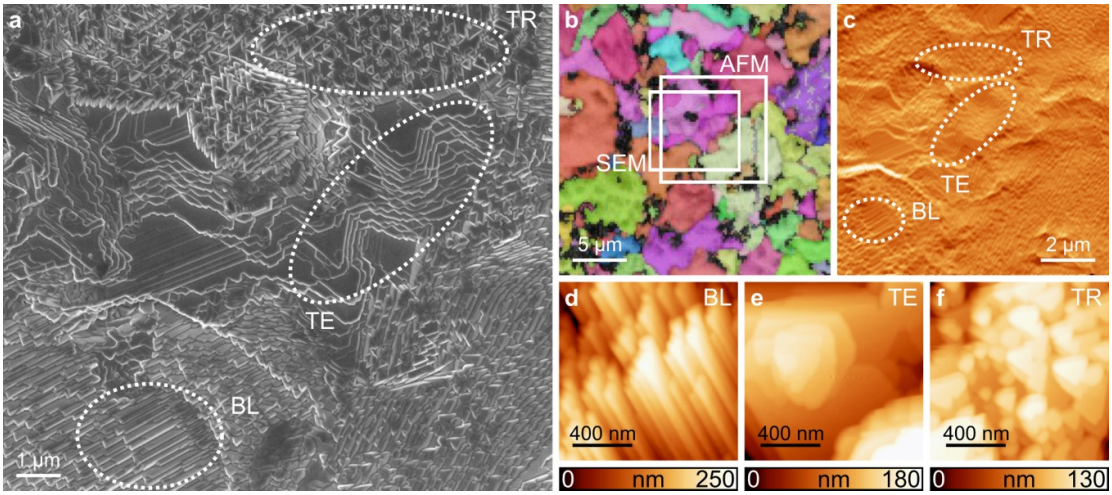

Figure 1. Different morphological features on the surface of CIGSSe thin films. (a) SEM image depicting basalt-like columns (BL), terraces (TE) and triangular (TR) features. (b) Overview EBSD map with the regions from where (a) SEM and (c) AFM images were obtained, marked by white squares. The 3 major morphological features are also found in the AFM image. Representative high resolution AFM images showing (d) BL, (e) TE and (f) TR morphologies.

marked in the SEM image are also found here. Representative high-resolution AFM images in figures 1(d)–(f) further display the three distinct features observable on the CIGSSe surface.

The BL columns resemble the highly facetted surfaces of epitaxially grown CISe thin films (on GaAs (001) and (110) substrates) that are known to facet into polar {112} planes as reported earlier [8, 22, 23]. An energetically favourable surface reconstruction resulting in a reduced surface Cu-content was found to be the reason for the high stability of these polar planes [24, 25]. Furthermore, Liao and Rockett detected triangular pyramids on the surface of epitaxially grown CIGSe films on $(111)_{cub}$ GaAs substrates [20]. These authors found that the surfaces of these triangular features also terminate in {112} planes.

In order to ascertain the crystallographic nature of the different morphological features detected in the current CIGSSe samples and to compare it with that of the well-studied S-free chalcopyrite absorbers, a combined analytical approach involving SEM, EBSD and AFM/STM techniques was pursued. The details for this correlative method are explained in sections 1 and 2 of the SI. In short, after locating the identical area in both EBSD and AFM images, the bulk crystal orientations of the grains at the surface (with respect to the normal to the substrate) in that specific area is deduced from the EBSD map. Due to pronounced surface facetting, the tilt angles θ of the surface planes with respect to the substrate normal can be determined by extracting line profiles from the AFM images (figure S2 in the SI). θ is also the angle between the individual facet orientation and the bulk grain orientation. Hence, knowing θ and the bulk crystal orientation, the surface facet orientation can be obtained. Practically, some of the known crystal planes in CIGSSe compounds are chosen and the angles to the bulk grain orientation are calculated. Unambiguous agreement in θ to the calculated values help to identify the specific surface plane (see table S2 in the SI). Furthermore, high-resolution STM topography images were used to determine the angles between smaller crystallographic facets present on all three morphologies.

Figure 2 depicts SEM/STM-based morphologies with the STM derivative, and the corresponding representations of the constituting surface facets of the three major morphological features. The combined analysis described above shows that the elongated BL columns are formed of polar {112} facets while their nano-faceted terminations are largely comprised of polar {100}/{001} surfaces (figure 2(a)). Interestingly, {112} planes are also found to dominate the triangular or hexagonal facets of the TE and TR morphologies (figures 2(b) and (c)). The sides of the TR are almost exclusively {112} facets (figure 2(c)) while the sides of the TE features are composed of both polar {112} and {100}/{001} facets. Therefore, all three morphologies (and thus the entire sample surface) are exclusively comprised of polar surfaces, with {112} facets comprising the majority of studied surfaces, followed by {100}/{001} facets. While some other types of polar surfaces such as {210}/{101}/{104} were also occasionally detected (see section 3 of the SI), no evidence for the occurrence of any non-polar {110}/{102} facets was found. This is in agreement with the fact that the non-polar surfaces in these chalcopyrites possess a significantly higher surface energy compared with the polar surfaces, as reported earlier by Liao and Rockett on CIGSe samples [23]. In contrast, it should be noted

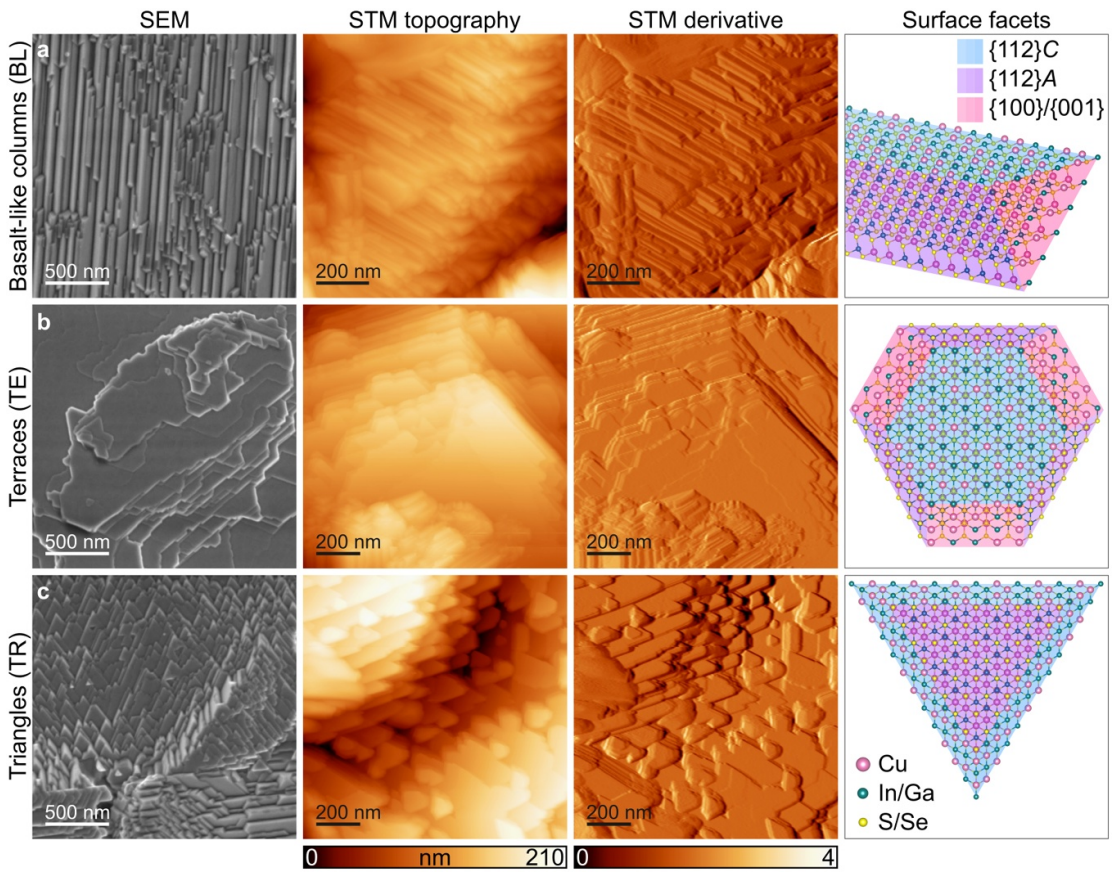

Figure 2. Correlating surface morphology and crystal facet terminations. Representative SEM image, STM topography ($U = +2.0$ V, $I = 0.23$ nA) and its derivative and the constituting surface facets of (a) BL, (b) TE and (c) TR morphologies. The surface facets were visualized using the Vesta software. The cation-terminated and anion-terminated {112} planes are denoted as {112}*C* and {112}*A* respectively.

that previously investigated polycrystalline CIGSe samples were found to consist of both non-polar and polar surface terminations [12].

Here it is noted that the difference between the S-free and S-containing samples compared in this work is not solely the sulfur content. They also differ in the growth process and overall chemical composition. The CIGSSe thin films studied in the current work were grown through magnetron sputtering of a Na doped Cu-In-Ga precursor layer, followed by the thermal evaporation of a Se capping layer and subsequent annealing by a rapid thermal processing approach under a S atmosphere [18]. On the other hand, the S-free polycrystalline CIGSe thin films previously exhibiting both polar and non-polar planes were grown using a multistage thermally activated coevaporation method [12, 15]. Differences in the nucleation rates and kinetics in these growth processes could be a factor leading to the formation of exclusively polar planes in the one case while not in the other. In addition, the samples also differ in their chemical composition, which can lead to differences in surface faceting. Considering the same growth process, the surface Cu-content in these S-containing absorbers could be another factor leading to the formation of {112} polar facets. Siebentritt *et al* had shown that the surface of Cu-poor ⟨001⟩ oriented CISe and CGSe with integral Cu content [Cu]/[In] = 0.6 and [Cu]/[Ga] = 0.8, respectively, both spontaneously faceted into polar {112} planes [22]. However, with increasing Cu content, this faceting was supressed. In the CIGSSe samples studied in the current work, the surface is significantly Cu depleted (relative Cu content with respect to group III elements [Cu]/[In]+[Ga] as quantified using XPS is 0.5 (figure S10 in the SI)), which could explain the occurrence of exclusively polar planes. The difference in the surface faceting could also be related to the difference in the surface Ga content among the two absorbers [26]. XPS measurements show a surface Ga content ([Ga]/[Ga]+[In]) of about 0.05 in CIGSSe while the CIGSe samples that we studied showed a Ga content of about 0.18 (figure S10). This indicates a severely Ga-depleted surface in CIGSSe effectively pointing towards a CISSe surface. According to the surface energy calculations by Shigemi *et al* with increase in the Ga content, the difference in the surface energy between polar and non-polar surfaces is reduced, which may lead to the formation of both types of planes in CIGSe while CIGSSe forms exclusively polar planes [26].

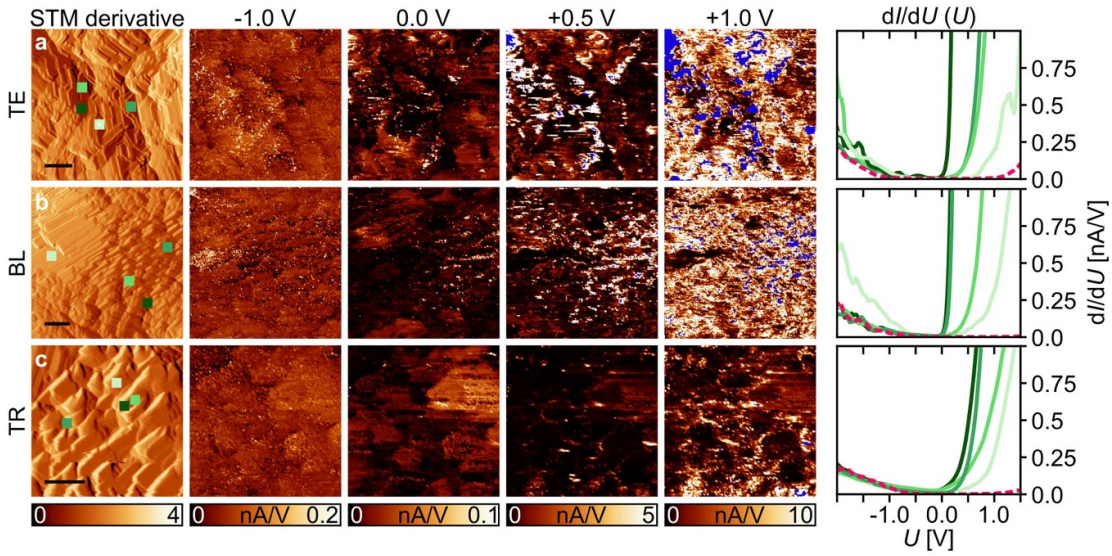

Figure 3. STM topography (derivative) and the corresponding CITS maps at −1 V, 0 V, 0.5 V and +1 V from areas with (a) TE, (b) BL and (c) TR morphologies. The scale bar for the STM images is 200 nm. From each area, an average of 36 dI/dU spectra as a function of the applied bias voltage U from the spots marked in the STM images are shown, indicating a highly defective surface. For reference, spectra from passivated surfaces showing semiconductor characteristics are depicted as dashed lines. All the STM images were obtained at $U = +2.0$ V, $I = 0.23$ nA while the CITS maps were obtained at $U = -2.3$ V, $I = 0.23$ nA in (a) and (b) and $U = -2.5$ V, $I = 0.23$ nA in (c). The blue areas in the CITS maps at $U \geqslant 0.5$ V indicate areas where the current limit of the measurement setup (5 nA) was exceeded.

The fact that three very distinct morphologies are detected despite the same constituting primary facets, can be associated with the integral orientation of the specific grain. Between the horizontal TE and TR features, the difference in morphology can be a result of various factors such as lateral differences in composition [27] or disparities in the nucleation rate between facets during the growth process [23, 28]. Another likely cause for the TE and TR features may be the difference in surface energies between cation-terminated ({112}C) and anion-terminated ({112}A) facets. Earlier reports on chalcopyrite-type absorbers show that {112}A surfaces have a significantly higher surface energy compared to the {112}C surfaces [26, 29, 30]. Therefore, grains terminating in {112}A surfaces may show a higher degree of faceting (specifically via the formation of lower-energy {112}C surfaces) than grains terminating in {112}C surfaces (for which faceting is suppressed), giving rise to the TR and TE morphologies (figure 2). This assertion is supported by SEM images showing that near steep changes in the sample topography, the {112}C-terminated sides of the TR may have a distinct TE-like appearance (see figure S6 in the SI).

Surface properties of chalcopyrite absorbers can have a significant effect on the growth behavior of buffer layers during device fabrication. The energy of absorber surface terminations, the lattice mismatch between the buffer and absorber layers, the type of atoms available for bonding at the absorber surfaces etc are possible factors that can influence the buffer layer growth [31, 32]. For example, Witte *et al* investigated the growth of 20–30 nm thick CdS and Zn(O,S) buffer layers grown using chemical bath deposition on co-evaporated polycrystalline S-free CIGSe thin films [15]. They found a non-contiguous growth of both buffer layers on polar {112} surface planes while dense buffers layers were found on polar {100}/{001} and non-polar {110}/{102} planes. They attributed this behavior to the low surface energy of {112} planes as well as the bonding partners for the nucleation of the buffers at the absorber surface. Extending these findings to the case of the current CIGSSe absorber, non-contiguous growth of the buffer layers on the commonly occurring {112} planes can be expected. This could have a detrimental impact on the overall device efficiency.

3.2. Surface defect physics

To examine the electronic defect density of the sample surface, several dI/d$U(U)$ maps were obtained in regions with morphologies that could be unambiguously identified. In figures 3(a)–(c), three exemplary data sets (one for each morphology) are shown. Each row consists of the derivative of the STM image of a specific morphology and the corresponding dI/dU-maps at selected bias voltages. For better understanding, 4 averaged dI/dU-spectra from the marked spots in each region are also shown.

An ideal semiconductor with a passivated surface is expected to show spectral characteristic similar to the dashed lines (red) in figure 3, with no defects states within the band gap. However, the CIGSSe surface is highly defective and displays strong lateral inhomogeneities in the defect density. The averaged dI/dU-spectra

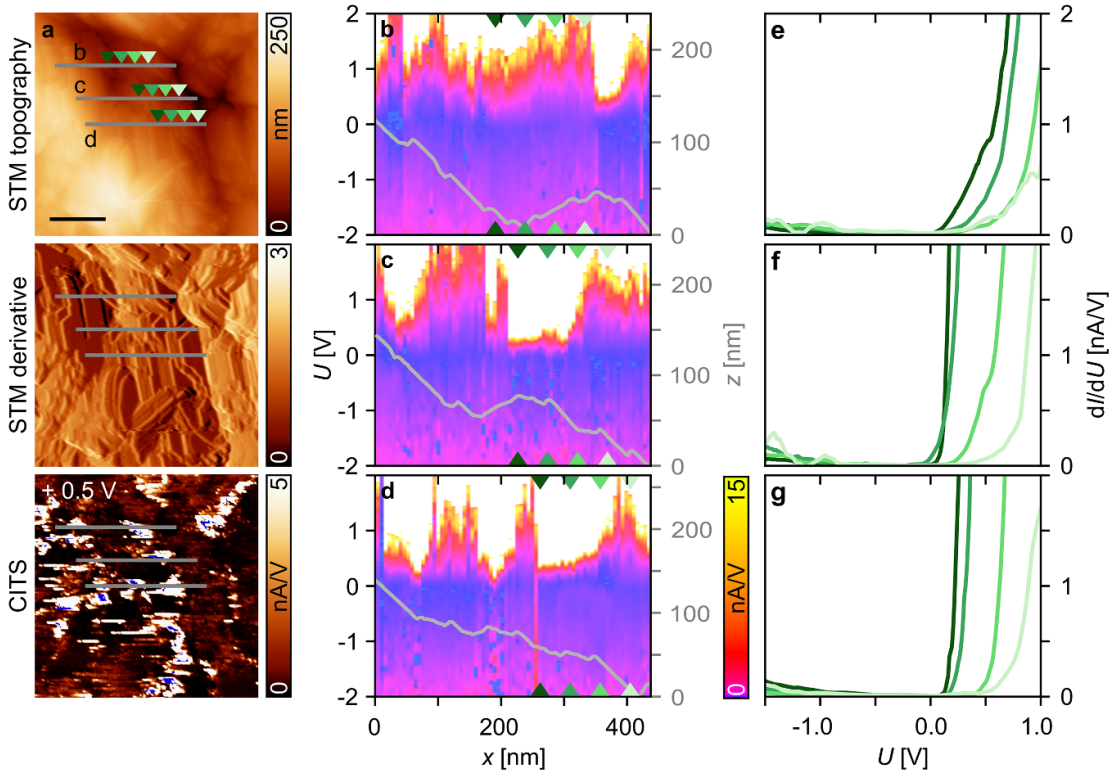

Figure 4. (a) STM topography, its derivative and the corresponding CITS map (at +0.5 (V) on CIGSSe depicting a surface with TE morphology. (b)–(d) Color coded dI/dU(U) spectra as a function of distance x along 3 different STM profiles (grey) across several terraces as indicated in (a). The topographic profiles (grey) are included in the color coded dI/dU map. (e)–(g) Selected single spectra, taken at the positions indicated by the green triangles in (a)–(d). The scale bar for the STM images is 200 nm. The measurement parameters were $U = +2.0$ V, $I = 0.23$ nA for the STM image and $U = -2.3$ V, $I = 0.23$ nA for the CITS map. The blue regions in the CITS map indicate areas where the current limit of the measurement (5 nA) was exceeded.

have a distinctly asymmetric appearance with a sharp increase in the differential conductance at positive bias voltages above the Fermi level. As reported earlier in selenide-based chalcopyrites, such a dI/dU signal is characteristic of an oxygen-induced surface dipole layer [8, 33]. This is a result of the easy diffusion of oxygen atoms into the subsurface of the chalcopyrite, leading to the displacement of Se atoms and related band gap defects. Such a mechanism can be assumed to also apply for the CIGSSe sample investigated in this study.

Before proceeding, it is essential that we differentiate between the intrinsic polarity of the polar lattice planes and the oxidation-induced dipole in these absorbers. The intrinsic polarity of these planes (for example {112}) arise due to the arrangement of the constituting anionic/cationic crystal planes. The high stability of such polar facets has been explained by an energetically favourable surface reconstruction that occurs in Cu-poor grown absorbers and that effectively compensates the intrinsic dipole. In particular, the cation terminated {112}C planes are stabilized by two Cu vacancies (2 V_{Cu}) per unit cell and the anion terminated {112}A surfaces by In on Cu antisite defects ($(In,Ga)_{Cu}$) [29, 34]. It should be noted that these defects do not lead to the formation of any band gap states [34]. The second type of surface dipole is formed as a result of surface oxidation and is known to also lead to the formation of detrimental electronic defect states within the band gap [8]. This O-induced dipole gives rise to the characteristic dI/dU spectra in the STS measurements with a steep increase at positive bias voltages (figure 3).

In polycrystalline CIGSe samples that terminate in both polar and non-polar facets, the polar {112} surfaces were found to be preferentially oxidized compared to the non-polar ones [12]. As the surface of the sample investigated in this study is comprised solely of polar surfaces, no such correlation can be made here. Nonetheless, a distinct lateral inhomogeneity in the surface electronic defect density which is independent of the specific facet terminations (i.e. {112} or {100}/{001}), can be detected. This finding warrants the need for further investigations to understand the origin of such variations.

Figure 4(a) shows the STM topography and its derivative, and the corresponding dI/dU map at $U = +0.5$ V of an area with TE morphology. The differential conductance as a function of distance along three lines (grey) over several terraces, step edges and trenches in the area and exemplary dI/dU spectra are also shown (figures 4(b)–(g)). For an easy correlation between the topography and the defect density, the STM

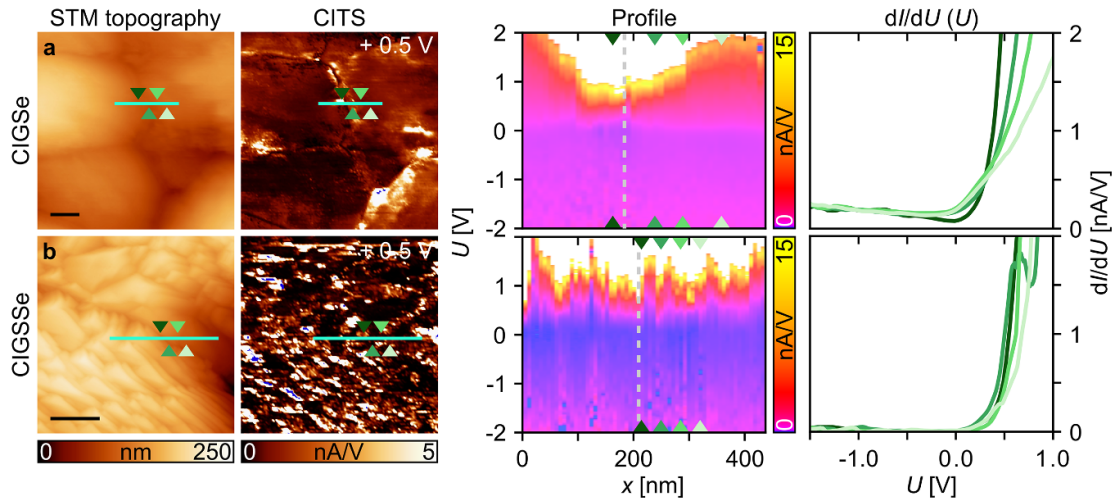

Figure 5. Difference in the GB effects in S-free and S-containing absorbers. STM topography, corresponding CITS map (at +0.5 (V), color coded dI/dU(U) spectra as a function of distance x along the profile (bright green) across a GB and selected single spectra from (a) CIGSe and (b) CIGSSe samples. A significant band bending is detected at the GB in CIGSe while such an effect is absent in CIGSSe. The scale bar for the STM images is 200 nm. The data in (a) was reprinted (adapted) with permission from [6]. Copyright (2015) American Chemical Society. The measurement parameters for the STM images were $U = -2.0$ V, $I = 0.40$ nA in (a) and $U = +2.0$ V, $I = 0.23$ nA in (b). The CITS maps were obtained at $U = -2.0$ V, $I = 0.40$ nA in (a) and $U = -2.7$ V, $I = 0.23$ nA in (b). The blue areas in the CITS map indicate areas where the current limit of the measurement (5 nA) was exceeded.

line profiles in each case are also included as grey lines in the color coded map. Despite the lateral differences in the differential conductance values throughout the area, no conclusive correlation between the surface electronic defect density and the sample topography could be made. Consequently, this indicates that the observations are not purely topographical effects, but rather linked to lateral differences in the surface defect level density.

On the surfaces of selenide-based chalcopyrite absorbers, GBs are known to exhibit inhomogeneities in the defect physics. Their distinct properties that are different and, often times, superior than the grain interior such as electronic passivation and downward band bending, have been well studied in the past [6, 13, 16]. The passivation effect is manifested in the form of a reduced dI/dU contrast around the Fermi level at GBs. An exemplary data set reproduced from the work by Bröker *et al* [6] is shown in figure 5(a). The differential conductance along the STM profile follows a distinct v-shape, centered approximately around the position of the GB as seen in the color coded waterfall plot of the corresponding dI/dU(U) spectra. Selected individual spectra clearly display the strong band bending effect while moving towards the GB (light to dark green spectra), indicating the shift of the corresponding defect states towards the Fermi level. In fact, GBs on the surface of these samples have been established to display band bending effects of up to ≈300 meV [13, 35].

To investigate the possible existence of GB effects in the CIGSSe sample studied in this work, a similar analysis was done. Figure 5(b) shows the STM topography and the CITS map (at 0.5 V) of a region containing 2 adjacent grains separated by a GB. Interestingly, no exclusive GB effects can be found here. In fact, the lateral inhomogeneities within each grain (especially at the edges of the morphological features in the bottom left grain) appear to exceed any potential GB effects. The strongest signatures of oxygen-induced dipoles are more often found at the edges of these topographical features, while areas with less corrugated topography show a lower differential conductance. Once again, this raises the question as to what the underlying causes for the lateral inhomogeneities in the surface electronic defect density on CIGSSe samples are.

The chemical composition of CIGSSe quinary compound is known to have a strong influence on its electronic structure. For example, Maeda *et al* observed a monotonic increase in the integral band gap with increase in both GGI and SSSe ratios [5]. Specifically, increasing the SSSe led to lowering of the VBM and raising of the CBM. By extension, it can also be expected that compositional changes near the sample surface have direct consequences on the surface defect physics in these materials. Surface sensitive XPS measurements in combination with GDOES indicated a higher S content at the surface compared to the bulk (see figure S10 (a)). To understand the role of elemental composition in causing the lateral differences in the surface defect density, electron dispersive x-ray (EDX) spectroscopy measurements were conducted. Figures 6(b)–(c) show color coded EDX maps of the three main morphological features at the surface depicting the S and Se content. The scale bar ranges from high Se/low S (blue) to high S/low Se (yellow) content. A significant lateral inhomogeneity in the chemical composition in the near surface region is detected. Specifically, there is a relatively higher S content at the edges of TE (figure 6(b)), terminations of BL

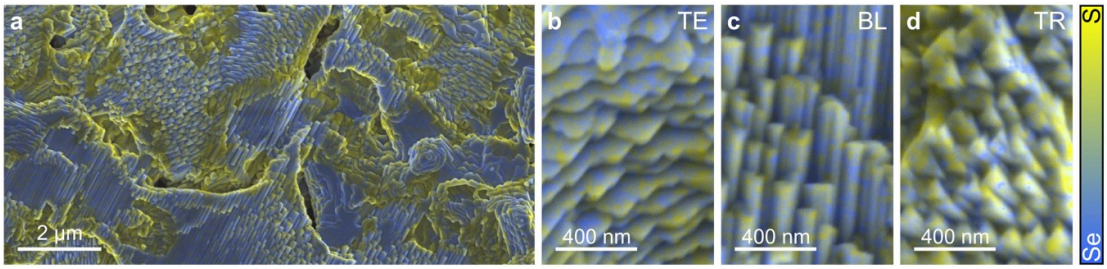

Figure 6. EDX maps of (a) a large-scale region of the surface of CIGSSe with multiple grains showing different morphologies as well as close-up images of (b) TE, (c) BL and (d) TR morphologies depicting the respective S and Se distributions.

(figure 6(c)) and corners of TR (figure 6(d)). In addition, S was also found to segregate on the morphological defects and GBs (figure 6(a)). For further details, see section 5 of the SI).

These inhomogeneities in the distribution of S and Se can be explained by differences in the Cu–VI and III–VI bond lengths [36, 37]. For example, consider the case of $CuInSe_2$ and $CuInS_2$. Cu–Se and In–Se bond lengths were found to differ by approximately 7%, while Cu–S and In–S bond lengths differed by around 10%, which can cause intrinsic strain in the $CuIn(S,Se)_2$ surface layers [36]. As a consequence, during the growth of the sample, it is expected that S segregates toward the GBs and topographic step edges by inter-diffusing with Se, thereby reducing the strain and ultimately giving rise to the differences in elemental distribution.

To some extend, the compositional differences correlate with the lateral inhomogeneities in the differential conductance in figure 5(b). In particular, the corners of the morphological features with high S content also exhibit the highest differential conductance with the tunneling current exceeding the detection limit (5 nA) of our measurement setup. This increased dipole characteristic may indicate a scenario where areas with high S content are easily oxidized compared to areas where there is a higher Se content. Another explanation for the observed effect is more technical and is related to the distance at which the STM tip is positioned over the surface. Due to the strong correlation between the chemical composition and electronic structure in CIGSSe as reported by Maeda *et al* the corners and edges of the morphological features with higher S content can have a higher band gap with respect to the S-poor areas in their interior [5]. Hence, the local DOS at the bias voltage at which the STM tip is approached to the surface can be different in different areas, resulting in the tip being closer to the surface in S-rich areas. At shorter tip-sample distances, the effect of the oxygen-induced surface dipole is more pronounced, leading to an increased dipole characteristic in the dI/dU-spectra. In this context, it is interesting that the GBs, despite a relatively higher S content, do not exhibit a significantly higher differential conductance with respect to the grain interiors.

3.3. Surface passivation by UHV annealing

The detrimental effects of surface oxidation on the electronic properties of the S-free chalcopyrite surfaces prompted the need for passivation strategies [11]. In selenide-based chalcopyrites, annealing to around 280 °C in UHV conditions was found to lead to removal of the oxidation-induced surface dipole and associated electronic defects, effectively passivating the sample surface [6, 8, 33]. Two other strategies that are known to exhibit similar passivation effects on the S-free chalcopyrite absorbers are Cd2+ preelectrolyte (CPE) treatment and heavy alkali metal PDTs [7, 38]. Boumenou *et al* showed that the CPE treatment can lead to the passivation of band gap states as depicted in the dI/dU characteristic and attributed this effect to an increase in the surface downward band bending and type inversion [7]. In an earlier work, we showed that the RbF PDT has the ability to protect the underlying CIGSe surface towards oxidation and associated electronic defects through the formation of an ultra-thin $RbInSe_2$-like layer [38]. Due to the isovalency of S and Se, we believe all these results obtained on S-free absorbers can be extended to S-containing CIGSSe absorbers.

The current CIGSSe samples were subjected to one of the above mentioned passivation strategies, i.e. heat treatment by annealing under UHV conditions, and the surface defect electronic properties were investigated. Figure 7 shows the dI/dU maps at specific bias voltages obtained from areas dominated by TE, BL and TR morphologies after UHV annealing. Irrespective of the area and type of surface facetting, the sample surface appears largely electronically passivated. In particular, the low differential conductance in the maps at 0 V and 0.5 V indicate the absence of defect electronic states within the band gap. This conclusion is supported by the averaged dI/dU-spectra, which invariably show the presence of a $\geqslant$1.5 eV wide band gap.

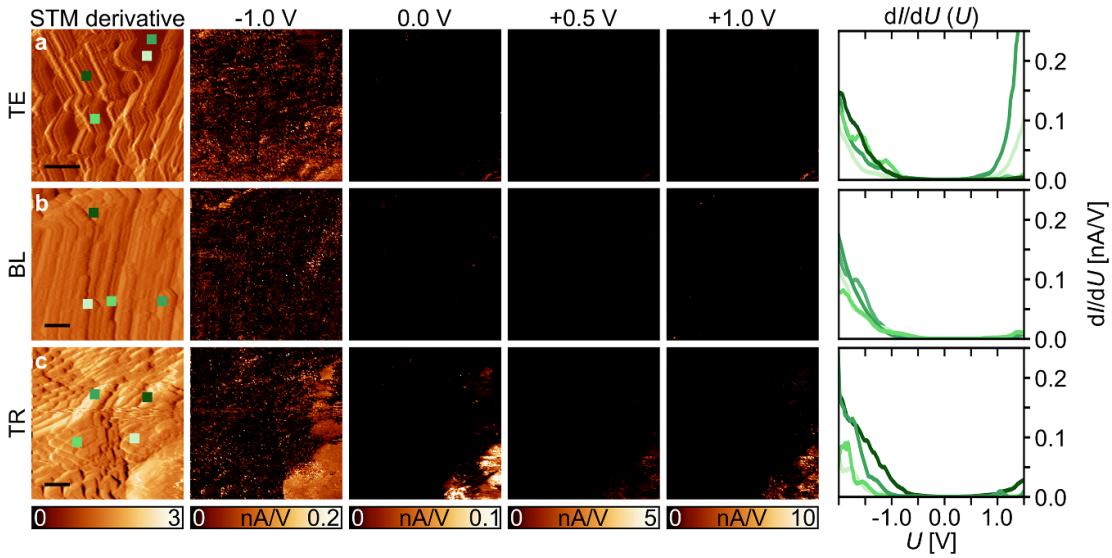

Figure 7. Passivating effect of UHV annealing. STM topography (derivative) and the corresponding dI/dU maps at −1 V, 0 V, 0.5 V and +1 V from areas with (a) TE, (b) BL and (c) TR morphologies. The scale bar for the STM images is 200 nm. In each area, averaged dI/dU(U) spectra as a function of the applied bias voltage U from the marked spots are also shown. The STM images were obtained at $U = +2.3$ V, $I = 0.18$ nA in (a) and $U = -2.7$ V, $I = 0.20$ nA in (b) and (c), while the CITS maps were obtained at $U = -2.7$ V, $I = 0.18$ nA in (a) and $U = -2.7$ V, $I = 0.20$ nA in (b) and (c). Note that the high differential conductance seen at the bottom right corner in (c) is attributed to a measurement artifact.

Specifically, no strong increase of the dI/dU-signal at positive bias voltages indicating the presence of oxygen-induced surface dipoles can be detected anymore, and the previously found lateral differences in differential conductance have been removed.

The advantageous surface passivation effect of heat treatment under UHV conditions has been extensively studied in S-free CISe/CIGSe chalcopyrites [6, 8, 33]. The oxygen atoms that diffuse into the subsurface were expelled during the UHV annealing (see figure S9 in the SI), removing the oxygen-induced surface dipole layer and associated defects. This mechanism can be assumed to hold true in the case of the current CIGSSe samples. Surface dipole-induced potential values were calculated based on the analysis in [8] for the state before and after annealing as shown in table S4 in the SI. A clear reduction in the potential after annealing the sample to 280 °C is found, indicating the removal of the oxygen-induced surface dipole. Interestingly, surface chemical composition quantified from XPS analysis indicate that the surface S content remains largely unaffected by the heat treatment (see figure S10(a) in the SI). To study the influence of heat on the distribution of the near-surface chemical composition, EDX measurements were also carried out on the UHV-annealed sample as shown in figure S12 in the SI. Apart from a slight decrease in the S and Ga contents, the results were found to be identical to the sample prior to the heat treatment. This implies that neither the surface chemical composition, nor differences in surface geometry between {112} and {100}/{001} terminations seem to have any influence on the surface passivation effect of UHV annealing.

Interestingly, XPS investigations carried out after each annealing step in a temperature series ranging from RT to 320 °C (see figure S10 in the SI) show some differences in the behavior of S-free and S-containing absorbers. The surfaces of S-free Cu-poor CISe and CIGSe samples are known to exhibit strong (beneficial) downward band bending after UHV annealing [6, 33], while such strong effects appear to be absent in the case of CIGSSe. For clarity, the XPS core-level binding energy shifts from previously reported CIGSe surface [6] and the current S-containing CIGSSe sample are plotted in figure S10(d) in the SI. A relative shift of ≈0.7 eV is detected after CIGSe undergoes heat treatment up to 320 °C. In comparison, there are no significant peak shifts in the CIGSSe case, indicating the absence of any heat-induced band bending. Surface chemical compositional analysis also shows slight differences between the two samples. While the surface Cu content in both cases evolve in a similar way with annealing temperature, Ga content exhibits slight variations as seen in figure S10(b) and (c) in the SI. Despite these differences, it is interesting that UHV annealing on both S-free and S-containing chalcopyrite absorbers lead to a similar passivation effect. We believe that by passivating the surface uniformly, this process can reduce recombination losses at the p/n-junction and enable the fabrication of high efficiency solar cells with significant reproducibility [11].

4. Conclusions

In summary, we characterized the surface of CIGSSe chalcopyrite absorber with a focus on the morphology and its correlation to the electronic defect physics. The surface is highly faceted and exhibits three distinct morphological features: basalt-like columns, terraces and triangles. A combined analytical approach using topographical analysis by AFM/STM and grain orientation determination by EBSD at the same location on the surface allows to identify the different facet terminations and their polarities. Unlike S-free chalcopyrite absorbers (CISe, CIGSe etc) that terminate in both polar and non-polar planes at the surface [12], CIGSSe surface is exclusively formed of polar planes. Defect density (dI/dU) mapping using STM-based CITS show a highly defective surface with significant lateral inhomogeneities, which could not be assigned to morphological differences and/or GB effects. The dI/dU spectral signature is indicative of an oxidation-induced surface dipole layer which can be removed by annealing the sample under UHV conditions (at around 280 °C). This surface passivation effect is similar to that detected earlier in S-free absorbers [8]. Our work provides a fundamental understanding of the surface defect electronic properties of CIGSSe surface and suggests a passivation strategy that can potentially be incorporated into the production process for improved device efficiencies.

Data availability statement

All data that support the findings of this study are included within the article (and any supplementary files).

Acknowledgments

A Elizabeth and H Mönig gratefully acknowledge financial support by the Deutsche Forschungsgemeinschaft (DFG) under the Project Number 387562434.

ORCID iDs

Amala Elizabeth https://orcid.org/0000-0003-1388-9112
Andreas May https://orcid.org/0009-0004-8349-1876
Finnegan Volkamer https://orcid.org/0009-0002-5515-9556
Florian Giesl https://orcid.org/0000-0001-9382-7880
Hossam Elanzeery https://orcid.org/0000-0001-6032-2499
Thomas Dalibor https://orcid.org/0000-0003-1178-6793
Daniel Abou-Ras https://orcid.org/0000-0003-3063-922X
Harry Mönig https://orcid.org/0000-0003-2639-9198

References

[1] Adhikari A, Acosta-Najarro D R, Fragoso-Medina A J, Reyes-Vallejo O, Cano F J, de la Luz Olvera Amador M and Subramaniam V 2024 Review on the developments in copper indium gallium diselenide (CIGSe)-based thin film photovoltaic devices *J. Mater. Sci.: Mater. Electron.* **35** 1016
[2] Keller J, Kiselman K, Donzel-Gargand O, Martin N M, Babucci M, Lundberg O, Wallin E, Stolt L and Edoff M 2024 High-concentration silver alloying and steep back-contact gallium grading enabling copper indium gallium selenide solar cell with 23.6% efficiency *Nat. Energy* **9** 467–78
[3] Dalibor T, Stölzel M, Elanzeery H, Aboulfadl H, Eraerds P, Borowski P, Reichel R, Didschuns I and Frankenberger H 2023 World record efficiency Cd-free CIGS modules and their advances for large-scale production *2023 Middle East and North Africa Solar Conf. (MENA-SC)* pp 1–5
[4] Touafek N and Mahamdi R 2014 Excess defects at the CdS/CIGS interface solar cells *Chalcogenide Lett.* **11** 589–96
[5] Maeda T, Nakanishi R, Yanagita M and Wada T 2020 Control of electronic structure in $Cu(In,Ga)(S,Se)_2$ for high-efficiency solar cells *Jpn. J. Appl. Phys.* **12** SGGF12
[6] Bröker S, Kück D, Timmer A, Lauermann I, Ümsür B, Greiner D, Kaufmann C A and Mönig H 2015 Correlating the local defect-level density with the macroscopic composition and energetics of chalcopyrite thin-film surfaces *ACS Appl. Mater. Interfaces* **7** 13062–72
[7] Boumenou C K, Babbe F, Elizabeth A, Melchiorre M, Spindler C, Guillot J, Mönig H, Siebentritt S and Redinger A 2020 Passivation of the $CuInSe_2$ surface via cadmium pre-electrolyte treatment. *Phys. Rev. Mater.* **4** 1–10
[8] Elizabeth A, Sahoo S K, Lockhorn D, Timmer A, Aghdassi N, Zacharias H, Kühne T D, Siebentritt S, Mirhosseini H and Mönig H 2020 Oxidation/reduction cycles and their reversible effect on the dipole formation at $CuInSe_2$ surfaces *Phys. Rev. Mater.* **4** 063401
[9] Valenta D *et al* 2024 The energy level alignment at the buffer/$Cu(In,Ga)Se_2$ thin-film solar cell interface for CdS and GaO_x *Adv. Mater. Interfaces* **11** 2301110
[10] Sharma D, Nicoara N, Jackson P, Witte W, Hariskos D and Sadewasser S 2024 Charge-carrier-concentration inhomogeneities in alkali-treated $Cu(In,Ga)Se_2$ revealed by conductive atomic force microscopy tomography *Nat. Energy* **9** 163–71
[11] Elizabeth A and Mönig H 2024 Identifying key parameters for reducing recombination losses at the p-n junction of chalcopyrite thin-film solar cells *PRX Energy* **3** 047001

[12] Elizabeth A, Conradi H, Sahoo S K, Kodalle T, Kaufmann C A, Kühne T D, Mirhosseini H, Abou-Ras D and Mönig H 2020 Correlating facet orientation, defect-level density and dipole layer formation at the surface of polycrystalline $CuInSe_2$ thin films *Acta Mater.* **200** 463–70

[13] Mönig H, Smith Y, Caballero R, Kaufmann C A, Lauermann I, Lux-Steiner M C and Sadewasser S 2010 Direct evidence for a reduced density of deep level defects at grain boundaries of $Cu(In,Ga)Se_2$ thin films *Phys. Rev. Lett.* **105** 116802

[14] Sadewasser S, Glatzel T, Rusu M, Jäger-Waldau A and Lux-Steiner M C 2002 High-resolution work function imaging of single grains of semiconductor surfaces *Appl. Phys. Lett.* **80** 2979–81

[15] Witte W, Abou-Ras D and Hariskos D 2013 Chemical bath deposition of Zn(O,S) and CdS buffers: influence of $Cu(In,Ga)Se_2$ grain orientation *Appl. Phys. Lett.* **102** 051607

[16] Azulay D, Balberg I and Millo O 2012 Microscopic evidence for the modification of the electronic structure at grain boundaries of $Cu(In_{(1-x)},Ga_x)Se_2$ films *Phys. Rev. Lett.* **108** 076603

[17] Boumenou C K, Phirke H, Rommelfangen J, Audinot J-N, Nishiwaki S, Wirtz T, Carron R and Redinger A 2023 Nanoscale surface analysis reveals origins of enhanced interface passivation in RbF post deposition treated CIGSe solar cells *Adv. Funct. Mater.* **33** 2300590

[18] Elanzeery H *et al* 2024 Beyond 20% world record efficiency for thin-film solar modules *IEEE J. Photovolt.* **14** 107–15

[19] Kodalle T *et al* 2019 Glow discharge optical emission spectrometry for quantitative depth profiling of CIGS thin-films *J. Anal. At. Spectrom.* **34** 1233–41

[20] Liao D and Rockett A 2008 The structure and morphology of (112)-oriented $Cu(In,Ga)Se_2$ epitaxial films *J. Appl. Phys.* **104** 094908

[21] Horcas I, Fernández R, Gómez-Rodríguez J M, Colchero J, Gómez-Herrero J and Baro A M 2007 WSXM: a software for scanning probe microscopy and a tool for nanotechnology *Rev. Sci. Instrum.* **78** 013705

[22] Siebentritt S, Papathanasiou N, Albert J and Lux-Steiner M C 2006 Stability of surfaces in the chalcopyrite system *Appl. Phys. Lett.* **88** 2005–7

[23] Liao D and Rockett A 2002 Epitaxial growth of $Cu(In,Ga)Se_2$ on GaAs(110) *J. Appl. Phys.* **91** 1978–83

[24] Liao D and Rockett A 2003 Cu depletion at the $CuInSe_2$ Surface *Appl. Phys. Lett.* **82** 2829–31

[25] Mönig H *et al* 2009 Surface Cu depletion of $Cu(In,Ga)Se_2$ films: an investigation by hard x-ray photoelectron spectroscopy *Acta Mater.* **57** 3645–51

[26] Shigemi A and Wada T 2012 Surface stabilities of various crystal faces of $CuInSe_2$ and related compounds by first principles calculation *Jpn. J. Appl. Phys.* **51** 10NC22

[27] Prot AJC M *et al* 2023 Composition variations in $Cu(In,Ga)(S,Se)_2$ solar cells: not a gradient, but an interlaced network of two phases *APL Mater.* **11** 101120

[28] Liao D and Rockett A 2002 Effect of surface orientation on the growth and properties of $Cu(In,Ga)Se_2$ *Conf. Record of the 29th IEEE Photovoltaic Specialists Conf.* pp 515–518

[29] Jaffe J E and Zunger A 2001 Defect-induced nonpolar-to-polar transition at the surface of chalcopyrite semiconductors *Phys. Rev.* B **64** 241304

[30] Zhang S B and Wei S H 2002 Reconstruction and energetics of the polar (112) and $(\bar{1}\bar{1}\bar{2})$ versus the nonpolar (220) surfaces of $CuInSe_2$ *Phys. Rev.* B **402** 081402

[31] Abou-Ras D, Kostorz G, Romeo A, Rudmann D and Tiwari A N 2005 Structural and chemical investigations of CBD- and PVD-CdS buffer layers and interfaces in $Cu(In,Ga)Se_2$-based thin film solar cells *Thin Solid Films* **480-481** 118–23

[32] Nakada T 2000 Nano-structural investigations on Cd-doping into $Cu(In,Ga)Se_2$ thin films by chemical bath deposition process *Thin Solid Films* **361** 346–52

[33] Mönig H, Lockhorn D, Aghdassi N, Timmer A, Kaufmann C A, Caballero R, Zacharias H and Fuchs H 2014 Heat induced passivation of $CuInSe_2$ surfaces: a strategy to optimize the efficiency of chalcopyrite thin film solar cells? *Adv. Mater. Interfaces* **1** 1300040

[34] Hinuma Y, Oba F, Kumagai Y and Tanaka I 2012 Ionization potentials of (112) and $(11\bar{2})$ facet surfaces of $CuInSe_2$ and $CuGaSe_2$ *Phys. Rev.* B **86** 1–7

[35] Rau U, Taretto K and Siebentritt S 2009 Grain boundaries in $Cu(In,Ga)(Se,S)_2$ thin-film solar cells *Appl. Phys.* A **96** 221–34

[36] Spiess H W, Haeberlen U, Brandt G, Räuber A and Schneider J 1974 Nuclear magnetic resonance in I_B–III–VI_2 semiconductors *Phys. Status Solidi* b **62** 183–92

[37] Mazalan E, Aziz M S A, Amin N A S, Ismail F D Roslan M S and Chaudhary K 2023 First-principles study on crystal structures and bulk modulus of $CuInX_2$ (X = S, Se, S-Se) solar cell absorber *J. Phys.: Conf. Ser.* **2432** 012009

[38] Elizabeth A *et al* 2022 Surface passivation and detrimental heat-induced diffusion effects in RbF-treated $Cu(In,Ga)Se_2$ solar cell absorbers *ACS Appl. Mater. Interfaces* **14** 34101–12